From discrete particles to solids - about sintering and self-healing

Stefan Luding

Multi Scale Mechanics, CTW, UTwente, POBox 217, 7500AE Enschede, NL

E-mail address of corresponding author: s.luding@utwente.nl

ABSTRACT

In this review, particulate materials are studied using the Discrete Element Method (DEM), where the particles keep their identity throughout. Loose particles can sinter due to time-, stress- or temperature-dependent forces. Large deformations of sintered samples will then lead to damage. Self-healing of damaged samples can be activated through re-sintering, a process that increases further the contact adhesion between particles.
Initially, the particle-samples are prepared by applying isotropic (hydrostatic) pressure. The spherical particles deform plastically at contact and stick to each other due to strong, non-linearly increased van der Waals forces. Such pressure-sintering results in a solid sample with (after releasing pressure) zero confining stress – on which uni-axial tension or compression can be applied.
Damage can occur through loss of contacts and/or loss of adhesion and more damage will occur with increasing deformation. In order to trigger "self"-healing at different damage levels, the mechanical loading is first stopped, second, the system is re-sintered (so that the adhesion at existing contacts in the damaged sample becomes stronger than originally), and third, mechanical loading is continued with the healed sample, in order to study the material properties after the healing event.

1. Introduction

Biological systems with their unique self-healing capability have inspired researchers to develop new engineering materials able to heal by themselves. One possibility is to initiate a bonding reaction at the crack faces, such that the defect disappears and the local strength of the material is re-established. At the atomic/molecular scale, bonding reactions can be triggered by increasing the mobility of atoms in the vicinity of the damaged zone. The necessary diffusion and bonding characteristics of the "healing agents" are realized by means of appropriate thermal and/or chemical processes (van der Zwaag, 2007).

Self-healing through chemical processes has been reported by White et al. (2001), who embedded brittle microcapsules filled with a liquid healing agent into an epoxy matrix. Healing is activated if a crack runs through the epoxy and breaks one of the microcapsules: the contained liquid flows out of the capsules into the cracked area, and glues the crack faces together (when getting into contact with a catalyst). This self-healing concept makes it possible to almost recover the original strength of the material. Other self-healing mechanism for polymers are related to the presence of non-covalent hydrogen bonds (Sijbesma et al., 1997) in the polymer network. The reversibility of the hydrogen bonds may induce a spontaneous rearrangement of chemical bonds that allow the polymer to adjust its new configuration to external stimuli and thus "self-heal".

Alternative to chemical processes, materials can heal by an input of external energy, such as heating, in order to trigger self-healing. Varley (2007) described the behaviour of ionomers after bullet penetration, where the required heat for healing directly comes from the impact energy. Self-healing paintings have been introduced recently in the automotive industry, where small scratches vanish after exposure to solar light and heating. More examples of state-of-the-art self-healing materials can be found in the recently published book edited by van der Zwaag (2007).

In this review the modeling of cohesive, sintering and self-healing particulate materials is reviewed. The mechanical evolution in time of all the particles in the material is simulated by means of the Discrete Element Method (DEM), where the discrete masses represent single particles and their interactions are simulated with a modern version of the sintering contact model (Luding, 2008) originally proposed by Luding *et al.* (2005). This contact model mimicks the physical behavior of the interaction of the particles accounting for dissipative, elasto-plastic, adhesive, and frictional effects. It is by construction non-linear in its response to external stresses (Luding, 2008). An additional temperature-dependence, as possibly resulting from diffusion of atoms and the resulting sintering effects, can be added on top of the elasto-plastic contact model (Luding et al., 2005).

The simplest self healing of particle contacts only involves the increase in contact strength due to re-sintering, without accounting in detail for all microscopic mechanisms involved. Experimental and numerical studies indicate that the net increase in strength depends on the sintering temperature and duration, see for example (Luding et al., 2005; Shoales and German, 1998; Takeuchi et al, 2002; Pirhonen et al., 2006). In the simulations, during the initial pressure sintering preparation, the optimal strength is not reached. Hence, the sample still has the potential to be strengthened further during a *second* sintering (healing). If the re-sintering is applied after the sample has already experienced some damage under mechanical loading (like uni-axial tension or compression), the question is to which extent the damage can be healed.

In Section 2 the simulation method is briefly summarized, and the pressure-sintering contact model is reviewed. Furthermore, the boundary conditions, the material parameters, and the preparation procedures for the particulate samples are explained. In Section 3, numerical results of DEM simulations are reviewed for damage under uni-axial tensile and compressive loading. Self-healing through sintering is then applied at different stages of deformation. Finally, in Section 4 the review is summarized and conclusions are drawn.

2. Simulation method

2.1 DEM modeling of particulate materials

The Discrete Element Method (DEM) for particle systems can be used to illustrate how the macroscopic response of a solid-like, sintered sample (as characterized by the yield strength, stiffness, dilatancy and anisotropy) depends on various microscopic properties, such as the contact network, the particle size, and the contact adhesion, friction, stiffness and viscosity (Herrmann et al., 1998; Vermeer et al., 2001; Liao et al., 2000; Luding and Herrmann, 2001; Suiker et al., 2001; Luding, 2004; Suiker and Fleck, 2004; David et al., 2005; Suiker and de Borst, 2005; Allen and Tildesley, 1997). Most of these microscopic properties will not remain constant during loading and depend also on stress and temperature.

In the present review, the coupling between micro- and macro scale properties is performed by first solving the equations of motion at the particle level, in a similar fashion as in the classical molecular dynamics approach, see the textbook by Allen and Tildesley (1997). The response of the particle system (expressed in terms of stress and strain) is obtained by averaging the local quantities at the particle contact level (forces and displacements) over the assembly. The effective response then depends directly on the chosen particle contact model (Thornton, 2000; Tomas, 2001; Luding, 2006; 2008). Even though recent studies have demonstrated that the accurate simulation of systems composed of non-spherical particles is

possible (Alonso-Marroquin et al., 2005; D'Addetta et al., 2002), for simplicity we restrict ourselves to spherical particles.

2.2 Sintering contact model

In the following, particulate material samples are (i) *prepared*, (ii) *deformed* and *damaged*, and then (iii) *self-healed* and (iv) *deformed* again. The non-linear contact model by Luding *et al.* (Luding, 2005; 2006; 2007; 2008; 2010; Luding and Suiker, 2008; Herbst and Luding, 2008; Mouraille et al., 2009; Luding and Bauer, 2010) is used – see these references for more details than sketched here. In figure 1, the normal contact force f (that is directed parallel to the line connecting the centers of two contacting particles) is plotted against the contact overlap, $\delta > 0$. If $\delta < 0$, there is no contact between particles, and thus $f = 0$. This sign convention relates positive (*negative*) values of the contact displacement δ to overlap/deformation (*separation*), while positive (*negative*) values of the contact force f relate to compression/repulsion (*tension/attraction*).
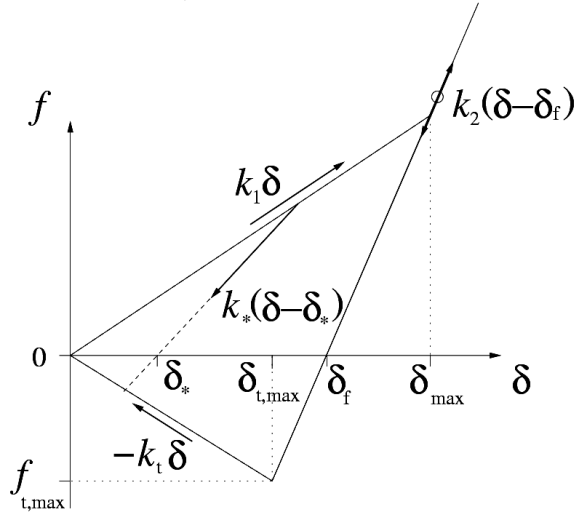

Fig. 1: Particle contact model plotted as force-displacement relation (Luding, 2005; 2008), with δ for contact positive, and repulsion and attraction forces positive and negative, respectively.

Starting from large distance, a contact begins at $\delta = 0$ and, during initial compressive loading, the contact force increases with the overlap as $f=k_1\delta$, with k_1 the elasto-plastic contact stiffness. When the external compressive forces are compensated by the contact repulsive force at the maximum contact overlap, δ_{max}, for unloading, the contact stiffness increases to a value k_2, so that the elastic unloading force is $f = k_2(\delta-\delta_f)$. Elastic unloading to zero contact force leads to the (plastic) contact overlap $\delta_f = (k_2-k_1)\,\delta_{max}/k_2$. If the overlap is further decreased, the contact force gets tensile, with maximum tensile contact force $f_{t,max} = -k_t\delta_{t,max}$, realized at contact displacement $\delta_{t,max} = k_2\delta_f/(k_2+k_t) = (k_2-k_1)\,\delta_{max}/(k_2+k_t)$. The tensile regime is an unstable branch, with the tensile contact force dropping from its maximum value towards zero in accordance with $f=-k_t\delta$.

For the sake of brevity, the tensile softening parameter k_t hereafter is referred to as the "contact adhesion". Note that, mostly for practical reasons (Luding, 2005; 2008), for contact deformations above δ_{max}, the force follows the limit branch $f = k_2(\delta-\delta_f)$, since further loading is unrealistic anyway and would lead to much stiffer behavior if properly modeled. In this "fluid" limit regime, the particles can be viewed as completely "melted" and stiffnesses as

large as those for "incompressible" fluids should be used – however, this would render the DEM simulation by orders of magnitude slower, so that we do not follow this path. Typically, the "fluid" overlap δ_f is chosen such that it corresponds to about 5% of the particle diameter, which is considered as "too large" contact deformation beyond the validity of the present model.

The extreme loading and unloading limit branches, are reflected by the outer triangle in figure 1. Starting from the realized maximal overlap, $\delta_{max}^* < \delta_{max}$, unloading occurs within the outer triangle, as characterized by a branch with stiffness $k_* = k_1 + (k_2 - k_1) \delta_{max}^*/\delta_{max}$, and (elastic, reversible) force, $f^* = k_*(\delta - \delta^*)$, with $\delta^* = (k_* - k_1) \delta_{max}^*/k_*$. The intermediate stiffness k_* follows from a linear interpolation between k_1 and k_2 – which is our (arbitrary) choice due to the lack of experimental data on this (probably) non-linear behavior. The corresponding maximal attractive force is $f_{t,max}^* = - k_t \delta_{t,max}^* = -k_t (k_* - k_1) \delta_{max}^*/(k_* + k_t)$. If we assume that the maximal overlap, δ_{max}, is realized under external (compressive) pressures, p_{max}, then one can infer $\delta_{max}^* = \delta_{max} (p/p_{max})$, with pressure $p = k_1 \delta_{max}^*/A$, with typical/representative area A. This leads to the realized maximal attractive force $f_{t,max}^* = -k_t (k_* - k_1) \delta_{max} (p/p_{max})/(k_* + k_t)$. Using $k_* = k_1 + (k_2 - k_1) (p/p_{max})$, one gets the possible attractive/cohesive stress $c = f_{t,max}^*/A$, which can be expressed as $c = -k_t (k_2 - k_1)(p_{max}/k_1)(p/p_{max})^2/(k_1 + k_t + (k_2 - k_1) (p/p_{max}))$, only a function of the material model constants, k_1, k_t, and k_2, the external stress, p, and the model inherent maximal stress, p_{max}. After some transformations, using $\Phi = p/p_{max} \leq 1$, $\kappa_1 = k_1/k_2 \leq 1$, and $\kappa_t = k_t/k_2$, leads to:

$$
\begin{aligned}
- c/p_{max} &= (k_t/k_1) (k_2 - k_1) \Phi^2/[k_1 + k_t + (k_2 - k_1) \Phi] \\
&= (\kappa_t/\kappa_1) \Phi^2/[\Phi + (\kappa_1 + \kappa_t)/(1 - \kappa_1)] \\
&= \Phi^2/[\Phi + (\kappa_1/\kappa_t + 1)/(1/\kappa_1 - 1)] = \Phi^2/[\Phi + 1/B] \\
&= B\Phi^2/[B\Phi + 1] \\
&\approx B\Phi^2 - B^2\Phi^3 + \dots ,
\end{aligned} \tag{1}
$$

with $B = (1/\kappa_1 - 1)/(\kappa_1/\kappa_t + 1)$. For linear elastic material models, $\kappa_1 = 1$, and implicitly $\kappa_t = 0$, as well as for cohesionless, plastic materials, $\kappa_1 < 1$, and $\kappa_t = 0$, one finds $c = 0$, as expected. For materials with elasto-plastic and adhesive contacts, $0 < \kappa_1 < 1$, and $\kappa_t > 0$, one finds the prefactors $B = 0$, 4/3, 2, 8/3, 20/7, 3, 20/6, 40/11, 50/13, 400/101, for, e.g., $\kappa_1 = 1/5$ and different $\kappa_t = 0$, 1/10, 1/5, 2/5, 1/2, 3/5, 1, 2, 5, 20, respectively. The "possible" macroscopic cohesion stress-ratio, $-c/p_{max}$, i.e., the healing potential, is thus (in leading order) proportional to the square of the previous confining pressure, with a pre-factor that increases with the contact adhesion.

In summary, the model has three ("stiffness") k-parameters that describe the three relevant physical effects at the contact: (1) elasticity, (2) plastic deformations, and (3) contact-adhesion. Furthermore, the model involves (4) a non-linear contact stiffness via the choice of k_*. This piece-wise linear model is a compromise between simplicity and the need to model physical effects. Except for some early theoretical studies, see (Tomas, 2001) and the many works that are based on it, there is no experimental/numerical literature available to our knowledge that provides enough detailed information on the force-displacement relations, involving all four physical contact properties above and their nonlinear, history-dependent behavior. If this information becomes available, the present model can be extended and generalized.

The *tangential contact force* acts parallel to the particle contact plane and is related to the tangential contact displacement through a linear elastic contact law, with the tangential stiffness k_s. The tangential contact displacement depends on both the translations and rotations of the contacting particles. Coulomb friction determines the maximum value of the tangential contact force: During sliding the ratio between the tangential contact force and the normal contact force is assumed to be limited and equal to a (constant) dynamic friction coefficient

μ_d; during sticking, the tangential force is limited by the product of normal force and static coefficient of friction μ_s. In a similar fashion, the elastic contact behavior related to rolling and twisting (torsion) is set by elastic constants k_r and k_o, respectively, and the maximum values of the corresponding contact torques depend on the normal contact force through a Coulomb-type law with "friction" coefficients μ_r and μ_o, respectively (Luding, 2008).

The overall solution of the non-linear DEM problem is obtained by incrementally solving Newton's equations of motion for the translational and rotational particle degrees of freedom. In the case of short-range particle interactions, which are present in particulate media such as powders and sands, a considerable decrease in computational time can be achieved using a linked-cell method that allows for a more efficient particle neighborhood search. Hence, this procedure is applied for the present simulations, and more details on the algorithm can be found, for example, (Allen and Tildesley, 1997).

3. Results

The simulations reviewed here consist of four subsequent stages, namely (i) a sample preparation stage (isotropic compression), (ii) a uni-axial (tensile or compressive) loading stage, (iii) a self-healing stage, and (iv) the continuation of the uni-axial loading. The samples are typically composed of about 10^3 poly-disperse spherical particles, with particle radii R_i either monodisperse, $R_i = \overline{R}$ (Luding, 2010; Luding and Bauer, 2010) drawn from a Gaussian distribution around mean $\overline{R}$ (Luding, 2006; 2008; David et al., 2005; Luding and Suiker, 2008; Herbst and Luding, 2008; Mouraille et al., 2009), or randomly homogeneously distributed between a minimum and a maximum (Luding, 2004; 2005; Luding and Herrmann, 2001).

3.1 Isotropic Loading – The Effect of Material Properties

In this section the results obtained from simulations of a "swelling" test are presented – which is equivalent, in the quasi-static limit, to slow isotropic mechanically driven compression or pressure increase (data not shown). The dependence of the packing density on the material parameters and the confining stress are examined. Here, the particles are initially randomly positioned on a square-lattice with low density, in a cubic system with periodic boundary conditions, in order to avoid wall effects. The system is first allowed to evolve to a disordered state, by attributing random velocities to all particles. The density is then increased by slowly increasing the particle size, while the system-volume $V = L^3$, with $L = 0.025$ m, is kept constant. The systems examined in the following contain $N = 1728$ particles with equal radii $a = \overline{R}$, where the use of the letter a indicates that the radius is a changing quantity. In the simulations (Luding, 2010; Luding and Bauer, 2010), the radii grow according to the relation $da/dt = g_r a$. The growth is stopped when a target volume fraction, v_{max}, is reached, where the volume fraction is defined as $v = NV(a)/V$, with the particle volume $V(a) = (4/3)\pi a^3$. The particle mass $m(a) = \rho V(a)$, with the fixed material density ρ, changes with the radius during the growth period. The volume fraction changes with time according to the relation $dv/dt = 3vg_r$, which leads to the volume fraction $v = v_0 \exp\{3g_r t\}$ as function of time t. The model parameters assumed are summarized in table 1. The particles correspond to spheres with initial radius $a_0 = 5\,\mu$m, growing up to a maximum radius of $a_{max} = 11.7\,\mu$m at volume fraction $v_{max} = 0.75$.

Tab. 1: Microscopic material parameters according to (Luding, 2008)

Property	Symbol	Values	SI units
Time Unit	t_u	1	$1\,\mu s$
Length Unit	x_u	1	10 mm
Mass Unit	m_u	1	1 mg
Particle radius	$a(t) = a_0 \exp(g_r t)$		
Initial particle radius	a_0	5.10^{-4}	5.10^{-6} m
Growth rate factor	g_r	0.02	2.10^{4} 1/s
Material density	ρ	2000	2000 kg/m³
Elastic stiffness	$k = k_2$	100	10^{8} kg/s²
Plastic stiffness	k_1 / k_2	0.2	
Adhesion "stiffness"	k_r / k_2	1.0	
Friction stiffness	k_s / k_2	0.2	
Rolling/torsion stiffness	$k_r / k_2 = k_0 / k_2$	0.2	
Plasticity range	ϕ_f	0.05	
Coulomb friction	$\mu = \mu_d = \mu_s$	1	
Rolling/torsion	$\mu_r = \mu_0$	0.1	
Normal viscosity	$\gamma = \gamma_n$	2.10^{-4}	2.10^{-4} kg/s
Friction viscosity	γ_f / γ	0.25	
Rolling viscosity	$\gamma_r / \gamma = \gamma_0 / \gamma$	0.25	
Torsion viscosity	$\gamma_0 / \gamma = \gamma_r / \gamma$	0.25	
Background viscosity	γ_b / γ	0.10	
Background torque	γ_{br} / γ	0.05	

Figure 2 shows the volume fraction v plotted as function of the dimensionless average swelling pressure pd/k_1, with $d = 2a$ in a semi-logarithmic representation. It is obvious that with an increase of the pressure the volume fraction increases. In particular the curves of figure 2(a) are obtained for different values of the friction coefficient at constant $\mu_r = 0.1$, and the curves of figure 2(b) are obtained for different values of rolling- and torsion-coefficients at constant $\mu = 1$. From figure 2(a) one concludes that small friction coefficients are always related to rather high densities, but increasing friction coefficients are not always sufficient to guarantee a decreasing packing density. The simulations almost collapse for $\mu \geq 1$. From figure2(b) one concludes that larger and larger rolling-/torsion- resistance leads to smaller densities, even though the curves with the largest coefficients almost collapse. Note that for higher pressures the influence of the friction coefficient and, even more clear, of the rolling-/torsion-coefficients on the volume fraction is smaller.
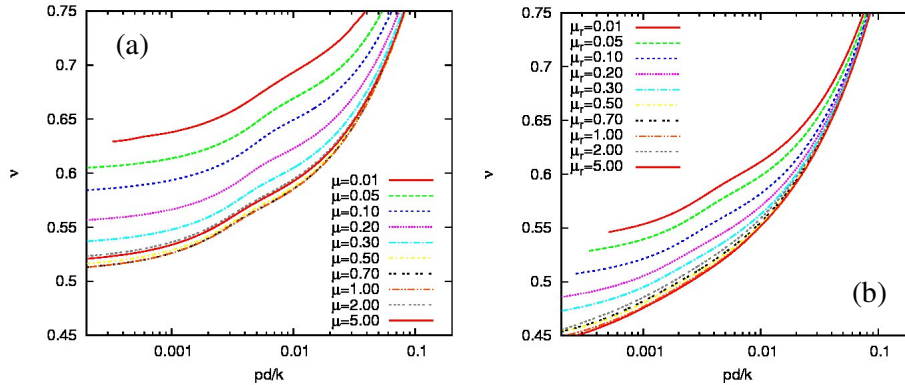

Fig. 2: Volume fraction plotted against the dimensionless pressure (scaled by k_1/d) for different values of (a) the friction coefficient, $\mu_r = 0.1$, and (b) the rolling-/torsion-coefficients, with $\mu = 1$.

3.2 Isotropic Loading – Sample Preparation

In the following, we focus on one set of material properties – corresponding about to the highest density in figure2(b) – and vary only the contact adhesion k_t. The radii R_i are now drawn from a Gaussian with mean $\overline{R} = 0.005$ mm (David et al., 2005; Luding, 2008). In contrast to the periodic boundaries in subsection 3.1, here six plane, perpendicular outer walls form a cuboidal volume, with side lengths of $L = 0.115$ mm. More detailed studies of the system size, different compression-rates and -methods, as well as different sintering procedures are beyond the scope of this review.

The material simulated represents a fine, stiff adhesive powder, with a particle size in the order of a few micrometers. The particle density used in the simulations is again ρ=2000 kg/m^3, the maximum elastic contact stiffness is k_2=5.10^4 N/m (which determines the fastest response time scale $t_c = \pi/\sqrt{k_2/m}$ of particles with mass m). The initial elasto-plastic stiffness (normalized by k_2) is k_1/k_2=1/2, and the contact adhesion k_t/k_2 is varied. The limiting "fluid-overlap" (Luding, 2005; 2008) for two contacting particles with radii R_1 and R_2 is computed as $\delta_f = \phi_f 2R_1R_2/(R_1+R_2)$, with the maximum plastic indentation strain, $\phi_f = 0.05$.

Tab. 2: Microscopic material parameters according to (Luding, 2008)

Property	Symbol	Values	SI units
Time Unit	t_u	1	1 ms
Length Unit	x_u	1	10 mm
Mass Unit	m_u	1	1 mg
Particle radius	$a(t) = a_0 \exp(g_r t)$		
Initial particle radius	a_0	5.10^{-4}	5.10^{-6} m
Growth rate factor	g_r	0	1/s
Material density	ρ	2000	2000 kg/m³
Elastic stiffness	$k = k_2$	5.10^4	5.10^4 kg/s²
Plastic stiffness	k_1/k_2	0.5	
Adhesion "stiffness"	k_t/k_2	[0, …, 1]	
Friction stiffness	k_s/k_2	0.2	
Rolling/torsion stiffness	$k_r/k_2 = k_0/k_2$	0	
Plasticity range	ϕ_f	0.05	
Coulomb friction	$\mu = \mu_d = \mu_s$	1	
Rolling/torsion	$\mu_r = \mu_0$	0	
Normal viscosity	$\gamma = \gamma_n$	5.10^3	5 kg/s
Friction viscosity	γ_f/γ	0.2	
Rolling viscosity	$\gamma_r/\gamma = \gamma_0/\gamma$	0.1	
Torsion viscosity	$\gamma_0/\gamma = \gamma_r/\gamma$	0.1	
Background viscosity	γ_b/γ	4	
Background torque	γ_{br}/γ	1	

The other stiffness parameters, friction coefficients, and viscous damping parameters are summarized in table 2. As a consistency check, we perform the simulations with a loading rate set to a factor of two smaller. The observed change in peak strength is rather small, so that we assume that the response is close to the quasi-static limit. As final remark, we note that the choice of parameters is empirical – most of them kept fixed here.

In (Luding and Kadashevich, 2007; Luding et al., 2007; Luding and Suiker, 2008; Herbst and Luding, 2008; Mouraille et al., 2009), the sample preparation was carried out subjecting a loose assembly of particles to (*isotropic*) *pressure sintering*, such that a coherent and solid particulate sample is obtained that subsequently is subjected to an *uni-axial tensile* or *compressive* test. The sample preparation by *pressure sintering* is characterized by two stages: The first stage reflects the application of a hydrostatic (or isotropic) pressure, $p_s/\sigma_0 =$

4.10^{-2}, to a loose assembly of particles, with the reference stress $\sigma_0 = k_1/(2\overline{R})$, where $\overline{R} = 0.005$ mm is the average particle radius. This desired isotropic stress is slowly applied to the six outer walls, which are considered to be virtually frictionless, i.e., $\mu_{wall} = 0.01$. The contact adhesion is set to zero ($k_{t,wall}/k_2 = 0$) for all particle-wall contacts, except for the particle-wall contacts in the direction of the uni-axial loading applied later (i.e., after the sample preparation phase has finished). For these walls, a relatively high contact adhesion of $k_{t,pull}/k_2=20$ is used in order to force the "wall particles" to directly follow the prescribed uni-axial deformation. During the application of the hydrostatic pressure, the value of the particle contact adhesion does not much affect the response, since most particles are loaded in compression, for more details see (Mouraille et al., 2009). The hydrostatic loading process is considered to be finished when the kinetic energy of the sample is negligible compared to the potential energy. For our sample, the solid volume fraction at the end of the hydrostatic loading process is $\nu = 0.676$ (which relates to a porosity of $1-\nu = 0.324$), and the average particle coordination number is $C = 7.17$. The volume fraction of this system is consistent with the one from the previous subsection, see the volume fraction in figure 2(b), at dimensionless pressure 0.04 and for the lowest rolling-resistance.

The second stage of the pressure sintering process is reflected by a *stress relaxation* phase, where the adhesion at *all* particle contacts is set to $k_t/k_2 = 1/5$, while the external hydrostatic pressure is strongly reduced to $p_s/\sigma_0 = 4.10^{-5}$. Due to the presence of particle contact adhesion, the lateral stability of the specimen remains preserved when the hydrostatic pressure is released, i.e., a coherent and stable particulate structure is obtained that can be subsequently used in the analysis of damage and healing under uni-axial loading conditions. The solid volume fraction of the sample after stress relaxation is decreased to $\nu = 0.63$ and the coordination number is now $C = 6.09$.

3.3 Response under uni-axial compression and tension

In the uni-axial compression (tension) test, one of the two outer walls, with its normal parallel to the axial (loading) direction, is slowly moved towards (away from) the opposite wall. The change of the wall displacement in time is prescribed by a cosine function with rather large period in order to limit inertia effects. Uni-axial tension is applied in a similar fashion by moving one of the two outer walls slowly away from the opposite wall. The connection between the "boundary particles" and the walls is artificially large, $k_{t,pull}$, at the two walls with normals in the loading direction. After some prescribed deformation, the sample is temporarily stopped, and self-healing is activated.

The response of the sample under uni-axial compression and uni-axial tension are shown in figure 3. The normal axial stress σ, normalized by the reference stress $\sigma_0 = k_1/(2\overline{R})$, is plotted as a function of the normal axial strain ε, where positive stress (*strain*) values relate to compression (*contraction*). The stress-strain curves are depicted for different values of k_t (normalized by k_2), which quantifies the adhesion at the particle contacts, see figure 1. A larger particle contact adhesion increases the effective strength of the sample, both under uni-axial tension and compression. Furthermore, the overall strain at which the effective stress reaches its maximum increases with increasing contact adhesion, k_t.
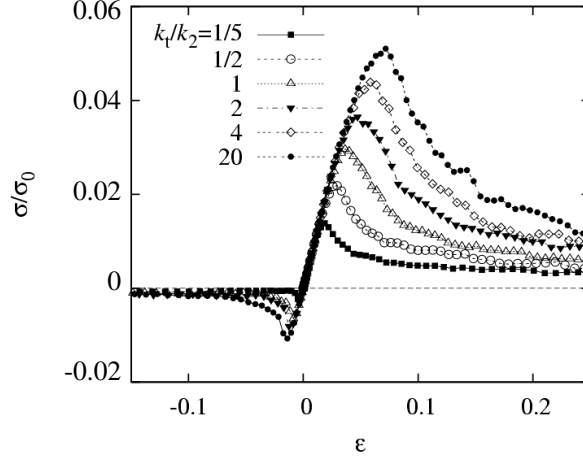
Fig. 3: Dimensionless axial stress (normalized by $\sigma_0 = k_1/(2\overline{R})$), plotted against axial strain during uni-axial compression (positive stress and strain values) and uni-axial tension (negative stress and strain values), for different particle contact adhesions k_t (normalized by k_2).

Note that the prediction on the available tensile force in Eq. (1) is not in agreement with the observed peak-strengths in figure 3 – probably due to the fact that an uni-axial deformation does not activate all available tensile forces in all directions equally. The maximum stress under uni-axial compression is order of five times larger than under uni-axial tension. A relatively high compressive strength in relation to the tensile strength is typical of various sintered materials, such as ceramics (Lee and Rainforth, 1995). As further result from figure 3, the softening branch under uni-axial tension is somewhat steeper than under uni-axial compression. For larger compression rates (data not shown), the system displays strong dynamic effects while for much smaller rates, the peak strength is not changed much for tension, but reduced a few per-cent for compression. Thus we use a rate here that is close to the quasi-static regime, as studied in more detail in (Herbst and Luding, 2008). The initial (elastic) axial stiffnesses C_t in tension and compression are determined by the sample preparation procedure, and are approximately equal for all the cases considered here, i.e., $C_t/\sigma_0 = 1.04$. The quantity C_t can be used to compare the present data with real experiments. The tensile responses are all characterized by local failure at the center of the sample. However, additional simulations (not presented here) have shown that local failure may also occur nearby one of the outer walls in the axial direction if the particle adhesion is equal or higher than the value $k_{t,pull}/k_2=20$ used for the "wall particles". In addition, changing the rolling and twisting friction parameters from $\mu_r =\mu_o=0.0$ to $\mu_r =\mu_o=0.2$ increased the tensile peak strength of the sample with about 20%, but a further increase of these friction parameters altered the tensile stress-strain response only little, see (Luding, 2008) for more details.

3.4 Self-healing under uni-axial compression and tension

During uni-axial compression, the sample is stopped at various strains, see figure 4 and the self-healing is achieved by an instantaneous increase of the particle contact adhesion k_t, which is assumed to be the net-effect of a re-sintering cycle. Technically, on the contact level, an increase of the contact adhesion k_t corresponds to an increase of the maximum tensile strength $f_{t,max}$, and a decrease of the corresponding displacement $\delta_{t,max}$. After the application of the re-sintering cycle (self-healing), uni-axial loading is resumed, where the effect of self-healing on

9

the effective stress-strain response of the sample becomes apparent through a comparison of its response with that of both, the unhealed reference sample and a pre-emptively healed sample, which has the stronger contact adhesion from the beginning on.

Under uni-axial compression, see figure 4(a), the self-healing of the initial sample with $k_t/k_2 = 1/5$ is activated by instantaneously increasing the contact adhesion to $k_t/k_2 = 1$, uniformly at all particle contacts. Figure 4 shows the response curves after the initiation of self-healing (dashed lines, labeled with the abbreviation 'SH'), together with the stress-strain responses of the relatively weak ($k_t/k_2 = 1/5$, solid squares) and strong ($k_t/k_2 = 1$, triangles) samples. The maximum compressive strength reached after self-healing is larger for healing at smaller deformation – and thus smaller damage. Astonishingly, for all self-healing cases considered, the response eventually converges to the response of the "strong" sample with $k_t/k_2 = 1$. The strong sample stress-response thus can be interpreted as the response of a pre-emptively "self-healed" sample, where the increase in contact adhesion is initiated at the onset of mechanical loading already. The response of the sample with $k_t/k_2 = 1$ acts as envelope for the responses of the self-healed samples with k_t/k_2 increased from 1/5 to 1.
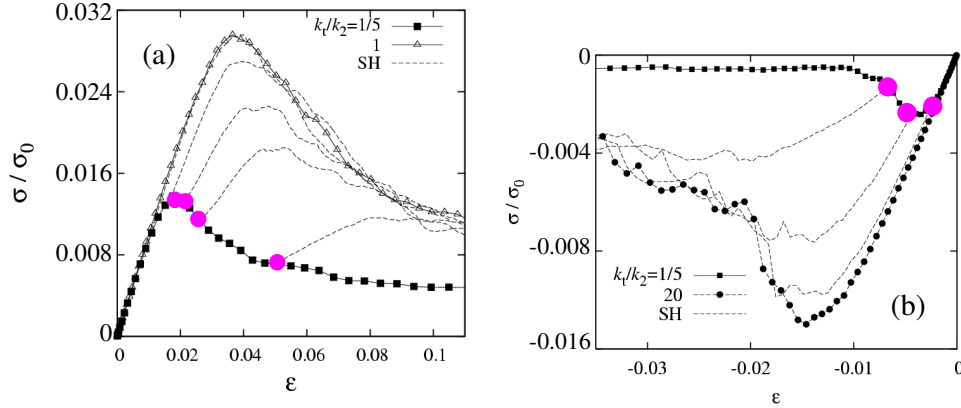

Fig. 4: Axial stress versus axial strain during (a) uni-axial compression and (b) uni-axial tension, for particle contact adhesions $k_t/k_2=1/5$ (solid squares). The initiation of self-healing occurs at axial strains $\varepsilon \approx 0.019$, 0.022, 0.026, and 0.045 for compression and $\varepsilon \approx -0.003$, -0.005, and -0.007 for tension, as indicated by (magenta) dots. The self healing strength is activated (a) five times and (b) hundred times larger than the original samples' contact adhesion. The self-healing stress responses are given (starting from the different strain points) by the dashed lines. The outer envelope corresponds to self-healing (increase of contact adhesion) already at zero strain.

In the case of uni-axial tension, self-healing is investigated by increasing the contact adhesion at various deformation levels from $k_t/k_2 = 1/5$ to $k_t/k_2 = 20$, see figure 4(b). Similar to the self-healing responses under uni-axial compression, the maximum tensile strength of the self-healed samples is larger if self-healing is initiated at smaller deformation. Also, the responses of the self-healed samples eventually coincide with the damage responses of the relatively "very strong" sample with $k_t/k_2 =20$. A comparison of the self-healing curves for different self-healing intensity (Luding et al., 2007; Herbst and Luding, 2008) confirms a stronger increase in contact adhesion leads to a higher overall sample strength.

In order to quantify the efficiency of self-healing, a dimensionless healing strength, $s=\sigma_{SH}/\sigma_{max}$, and healing strain, $e=\varepsilon_{SH}/\varepsilon_{max}$, were introduced by Luding and Suiker (2008). The self-healing strength is maximal for small strains, i.e., $s \approx 1$ for $e<0.5$, and gradually drops to a value of about 0.4 for strain values between $0.5<e<1.5$. Accordingly, in order to (almost) recover the maximum strength of the original reference sample, the global self-healing, as applied here, needs to be activated quite early in the fracture process. The self-healing efficiency was found to depend only marginally on the direction of uni-axial loading. However, for large deformations $e>1.5$ a noticeable difference is expected, since samples

loaded under uni-axial compression reach a finite residual strength under continued deformation, whereas samples loaded in uni-axial tension will eventually break completely, i.e., will end up with zero residual strength.

The self-healing model was further detailed and also applied locally and with time-dependence, as reported by Herbst and Luding (2008). Self-healing was applied locally dependent on the *local* strain and thus *local damage*. Technically, single contacts were healed when they fulfilled certain conditions like, e.g., being close to the tensile failure force, i.e., the maximal adhesive strength allowed.

4. Conclusions

In this review, (1) isotropic preparation, (2) uni-axial deformation, and (3) self-healing processes in damaged particulate materials have been studied using DEM simulations. The effect of self-healing is mimicked by a (global) sintering process, as modeled by increasing the particle contact adhesion from relatively "weak" to rather "strong".

(1) Isotropic preparation was chosen, since only then one can hope to create a homogeneous, isotropic packing. The question is at which pressure will the packing have a certain volume fraction (density). Different material properties, like contact-friction and rolling resistance affect this behavior and for low pressures, densities were realized in the range between volume fractions 0.44 and 0.64. The lowest densities are realized for large friction *and* large rolling/torsion resistance, while the highest densities are realized for practically frictionless systems – close to the random-close-packing density 0.64. With increasing pressure, density increases in general and the range of variation of densities decreases. As important result, we observe that another independent simulation with other parameters still leads to the same dependence on dimensionless quantities, so that the detailed parameter study can be used as a prediction for other results if dimensionless quantities are considered.

(2) Using one particular packing from the isotropic preparation, stress was released and uni-axial compression/tension was applied for different contact adhesion strengths. While the compression modulues (slope of the stress-strain curves) is not much affected, the peak strength of the material is: The stronger the contact adhesion, the larger the peak strength. For compression, the strength appears about a factor of five larger than for tension and the softening branch is rather smooth for compression, while the tensile regime shows a sharper drop, resembling more brittle-like behavior.

(3) At different strains, the uni-axial deformation is stopped and global self-healing is applied. The stress-strain response obtained from such self-healed samples eventually converges to the envelope curve that represents the damage response of a sample that has the "strong" contact adhesion since the onset of loading. This feature is astonishingly independent of the deformation level at which the self-healing mechanism is activated. Another result is that the maximum sample strength reached after self-healing very much depends on the deformation level at which self-healing is activated: If self-healing is activated before the peak-stress is reached, the maximum sample strength will be (virtually) equal to the peak strength of the envelope curve. In contrast, if self-healing is initiated in the softening regime, the sample strength is considerably smaller than the maximum reference strength. Hence, for optimal strength recovery, the healing mechanism should be activated as early as possible, before the sample reaches its peak strength and gets into the softening regime.

ACKNOWLEDGEMENTS

References

Allen, M. P., Tildesley, D. J., 1987, *Computer Simulation of Liquids*, Oxford University Press, New York.

Alonso-Marroquin, F., Luding, S., Herrmann, H. J., and Vardoulakis, I., 2005, *Role of anisotropy in the elastoplastic response of a polygonal packing*, Phys. Rev. E **71**, 051304.

D'Addetta, G. A., Kun, F., Ramm, E., 2002, *On the application of a discrete model to the fracture process of cohesive granular materials*, Granular Matter **4**(2), 77-90.

David, C. T., Garcia-Rojo, R., Hermann, H. J., Luding, S., 2005, *Hysteresis and Creep in Powders and Grains*, in: *Powders and Grains 2005*, R. Garcia Rojo, S. McNamara, and H. J. Herrmann (eds.), Balkema, Netherlands, pp. 291-294.

Herbst, O., Luding, S., 2008, *Modelling particulate self-healing materials and application to uni-axial compression*, Int. J. of Fracture 154, 87-103.

Herrmann, H. J., Hovi, J. P., Luding, S. (Eds.) 1998, *Physics of Dry Granular Media*, NATO ASI Series E 350, Kluwer Academic Publishers, Dordrecht, Netherlands.

Lee, W. E., Rainforth, W. M., 1995, *Ceramic Microstructures, Property Control by Processing,* Chapman and Hall, London, UK.

Liao, C. L., Chan, T. C., Suiker, A. S. J., Chang, C. S., 2000, *Pressure-dependent elastic moduli of granular assemblies*, International Journal for Numerical and Analytical Methods in Geomechanics **24**, pp. 265-279.

Luding, S., 2004, *Micro-macro transition for anisotropic, frictional granular packings*, International Journal of Solids and Structures **41**, 5821-5836.

Luding, S., 2006, *About contact force-laws for cohesive frictional materials in 2D and 3D*, in: *Behavior of Granular Media*, P. Walzel, S. Linz, Ch. Krülle, and R. Grochowski (eds.), Band 9, Schriftenreihe Mechanische Verfahrenstechnik, ISBN 3-8322-5524-9, Shaker Verlag, Aachen, pp. 137-147.

Luding, S., 2008, *Cohesive, frictional powders: contact models for tension*, Granular Matter **10**, pp. 235-246.

Luding, S., 2010, *Isotropic compression of cohesive-frictional particles with rolling resistance*, in: Numerical Methods in Geotechnical Engineering, (NUMGE2010 Proceedings, 2010), T. Benz and S. Nordal (Eds.), CRC Press/Balkema, NL, ISBN: 978-0-415-59239-0, pp. 219-224.

Luding, S., and Bauer, E., 2010, *Evolution of swelling pressure of cohesive-frictional, rough and elasto-plastic granulates*, in: Geomechanics and Geotechnics: From Micro to Macro, (IS-Shanghai Conference Proceedings, 11.-12. Oct. 2010), M. Jiang, L. Fang, and M. Bolton (Eds.), CRC Press/Balkema, NL, ISBN: 978-0-415-61295-1, pp. 495-499.

Luding, S., Herrmann, H. J., 2001 , *Micro-Macro Transition for Cohesive Granular Media*, in: *Zur Beschreibung komplexen Materialverhaltens*, Institut für Mechanik, S. Diebels (Ed.), Stuttgart, Germany, pp 121-134.

Luding, S., Kadashevich, I., 2007, *From weak powders to strong solids,* PARTEC 2007, Nuremberg, Germany, 4 pages, CD Proceedings.

Luding, S., Manetsberger, K., Muellers, J., 2005, *A discrete model for long time sintering*, Journal of the Mechanics and Physics of Solids **53/2**, pp. 455-491.

Luding, S., Suiker, A., 2008, *Self-healing of damaged particulate materials through sintering*, Philosophical Magazine **88** (28-29), 3445-3457.

Luding, S., Suiker, A., Kadashevich, I., 2007, *Discrete element modeling of self-healing processes in damaged particulate materials,* in: Proceedings of the 1st International Conference on Self Healing

Materials, 18-20 April 2007, Noordwijk aan Zee, The Netherlands, ISBN 978-1-4020-6249-0, A. J. M. Schmets and S. van der Zwaag (Eds.), Springer Series in Material Science 100.

Mouraille, O., Herbst, O., Luding, S., 2009, *Sound propagation in isotropically and uni-axially compressed cohesive, frictional granular solids*, Engineering Fracture Mechanics **76**, 786-791.

Pirhonen, E., Moimas, L., Väänänen, P., 2006, *Porous bioactive glass scaffold with high compression strength*, European Cells and Materials **12**, Suppl. 1, pp. 67.

Shoales, G. A., German, R. M., 1998, *In situ strength evolution during the sintering of bronze powders*, Metallurgical and Materials Transactions A **29a**, pp. 1257-1263.

Sijbesma, R. P., Beijer, F. H., Brunsveld, L., Folmer, B. J. B., Hirschberg, J. H. K., Lange, R. F. M., Lowe, J. K. L., Meijer, E. W., 1997, *Reversible polymers formed from self-complementary monomers using quadrupole hydrogen bonding*, Science **278**, pp. 1601-1604.

Suiker, A. S. J., de Borst, R., 2005, *Enhanced continua and discrete lattices for modeling granular assemblies*, Phil. Trans. Royal Society A **363**, pp. 2543-2580.

Suiker, A. S. J., Fleck, N. A., 2004, *Frictional collapse of granular assemblies*, Journal of Applied Mechanics **71**, pp. 350-358.

Suiker, A. S. J., Metrikine, A. V., de Borst, R., 2001, *Comparison of the wave propagation characteristics of the Cosserat continuum model and corresponding discrete lattice models*, Int. Journal of Solids and Structures **38**, pp. 1563-1583.

Takeuchi, T., Kondoh, I., Tamari, N., Balakrishnan, N., Nomura, K., Kageyama, H., Takeda, Y., 2002, *Improvement of mechanical strength of 8 mol % Yttria-stabilized zirconia ceramics by spark-plasma sintering*, Journal of The Electrochemical Society **149**, pp. A455-A461.

Thornton, C., Antony, S. J., 2000, *Quasi-static deformation of a soft particle system*, Powder Technology **109,** 179-191.

Tomas, J., 2001, *Assessment of mechanical properties of cohesive particulate solids – part 1: particle contact constitutive model*, Particle Science Technology **19**, 95-110.

Van der Zwaag, S., 2007, *An introduction to material design principles: Damage prevention versus damage management*. in: *Self Healing Materials. An Alternative Approach to 20 centuries of Materials Science*, S. Van der Zwaag, ed., Springer, Dordrecht, The Netherlands, 2007, pp. 1-18.

Varley, R., 2007, *Ionomers as self healing polymers* in: *Self Healing Materials. An Alternative Approach to 20 centuries of Materials Science*, S. Van der Zwaag, ed., Springer, Dordrecht, The Netherlands, pp 95-114.

Vermeer, P. A., Diebels, S., Ehlers, W., Herrmann, H. J., Luding, S., Ramm, E. (Eds.), 2001, *Continuous and Discontinuous Modelling of Cohesive Frictional Materials*, Lecture Notes in Physics 568, Springer, Berlin, Germany.

White, S. R. Sottos, N. R., Geubelle, P. H., Moore, J. S., Kessler, J. S., Sriram, S. R., Brown, E. N., Viswanathan, S., 2001, *Autonomic healing of polymer composites*, Nature **409**, pp. 794-797.